Materials Reports Solidwaste & Ecomaterials

Materials Reports: Solidwaste and Ecomaterials

Journal Homepage: www.sciopen.com/journal/3078-4093

Original Research Report

Mechanical behavior and microstructure evaluation of eco-friendly mortar containing ceramic wastes

Shibo Sun [1, §], Haoran Jia [1, §], Xiaochuan Hu [2], Linsheng Li [2], Xinyu Wang [1], Sha Qing [1], Le Li [1, *]

[1] School of Engineering and Technology, China University of Geosciences, Beijing 100083, China

[2] Department of Civil Engineering, Tsinghua University, Beijing 100084, China

Abstract: This study explores the partial substitution of cement and natural sand with ceramic waste in cement-based materials. Seven mixtures were prepared at a constant water-to-binder ratio of 0.4, with 20% cement replaced by ceramic powder and five levels of ceramic aggregate substituting natural sand. Compressive strength was evaluated through mechanical testing at curing ages of 7, 28, 90, and 180 d. Hydration products and phase evolution of the blended pastes were characterized using thermogravimetric (TG) and X-ray diffraction (XRD) analysis, while pore structure was assessed by dynamic vapor sorption (DVS) and mercury intrusion porosimetry (MIP) tests. The results indicate that: (1) replacing up to 60% of sand with ceramic aggregate does not adversely affect long-term compressive strength, despite an observed reduction compared to the reference mortar at early curing ages; (2) the progressive decrease in calcium hydroxide ($Ca(OH)_2$) content over time provides direct evidence of the pozzolanic activity of ceramic waste; (3) with increasing ceramic content, the fraction of fine capillaries decreases while larger gel pores increase, indicating nanoscale pore structure coarsening. These results provide a theoretical and experimental basis for the practical application of ceramic waste in high-performance cementitious composites.

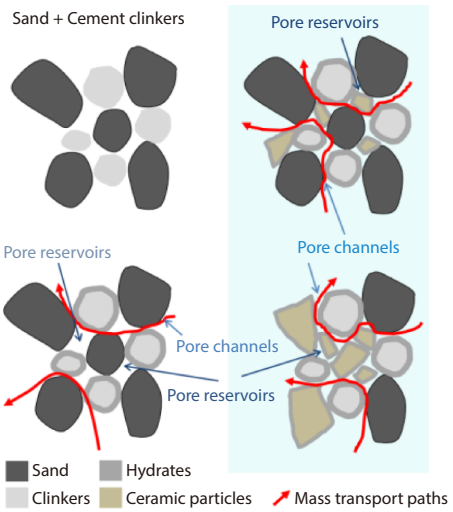

Keywords: ceramic wastes, compressive strength, pore structure, sustainability

Citation: S. Sun, H. Jia, X. Hu, et al. Mechanical behavior and microstructure evaluation of eco-friendly mortar containing ceramic wastes. *Materials Reports: Solidwaste and Ecomaterials*, 2026, 2: 9520028. https://doi.org/10.26599/MRSE.2026.9520028.

1. Introduction

Concrete is widely recognized as one of the most extensively utilized construction materials globally. Its prevalence stems primarily from its cost-effectiveness, favorable mechanical performance, satisfactory durability, and ease of placement, enabling its adaptation to diverse forms and structural configurations[1-3]. Nevertheless, the manufacturing process of Portland cement—the principal binder in concrete—is characterized by substantial energy consumption and considerable environmental impact, chiefly due to elevated carbon dioxide emissions[4,5]. In light of these concerns, considerable research efforts have been directed toward mitigating such adverse effects through the incorporation of alternative pozzolanic materials as partial replacements for cement[6-8]. This strategy not only holds potential for enhancing certain material properties but also contributes to environmental sustainability and economic efficiency by reducing industrial waste, energy usage, and production costs[9].

Ceramics are conventionally produced by blending and fir-

§S. Sun and H. Jia contributed equally to this work

*Correspondence to L. Li, lile@cugb.edu.cn

Received 8 April 2026; Received in revised form 22 April 2026; Accepted 3 May 2026

ing raw materials such as clay, feldspar, and quartz[10,11]. It is estimated that approximately 30% of the ceramic industry's daily output ultimately becomes waste, the majority of which remains unrecycled through effective means[12]. The continual accumulation of ceramic waste imposes significant pressure on related industries to develop sustainable disposal strategies. In response, previous studies have explored ceramic waste as a substitute for fine or coarse aggregate[13-15] or as a partial cement replacement[16–19]. Zhang et al.[20] reported 26.5% and 15.5% increases in flexural and compressive strength, respectively, with full replacement of natural fine aggregate by ceramic aggregate. Conversely, Pokorný et al.[16] observed reductions in compressive strength, flexural strength, and thermal properties following the incorporation of ceramic powder, alongside improved thermal insulation. Vejmelková et al.[17] noted that ceramic powder delayed compressive strength development, with 28-day strength reaching approximately 90% of that of the reference concrete. Similarly, Heidari and Tavakoli[18] documented a decline in early-age compressive strength with increasing ceramic powder content, although the reduction became less pronounced at later stages. Cheng et al.[21] found that replacing 10%–40% of cement with ceramic powder reduced concrete permeability, while another work[22] indicated diminished carbonation resistance but enhanced resistance to sulfate attack.

Despite these findings suggesting that ceramic waste can be effectively incorporated into concrete without significant detriment to mechanical or durability performance, systematic microstructural investigations remain limited. A thorough understanding of ceramic materials—particularly the synergistic effects of ceramic powder and aggregate on cement hydration and strength development—is essential for optimizing mix designs and ensuring long-term reliability.

In this context, the present study utilizes ceramic powder and ceramic aggregate as partial replacements for cement and natural sand, respectively, in cement-based composites. The primary objective is to investigate the effects of ceramic-based materials on compressive strength, hydration behavior, and pore structure, contributing to the sustainable utilization of ceramic waste in construction applications.

2. Materials and experiments

2.1. Materials

Waste ceramics were processed into fine aggregate and powder, and ordinary Portland cement was employed as the binder. Table 1 summarizes the chemical compositions of both the ceramic materials and cement, and their respective particle size distributions are illustrated in Fig. 1. The mineral composition of the cement, determined via Bogue's procedure, comprised C_2S (21.23%), C_3S (56.59%), C_3A (7.47%), C_4AF (8.89%), and other phases (5.82%).

The waste ceramics originated from discarded ceramic products obtained from a local enterprise in Jiangxi Province, China. A portion of the ceramics was dried and ground to achieve an average specific surface area (SSA) of 458 $m^2 kg^{-1}$. As illustrated in Fig. 1, the ceramic powder exhibited greater fineness than cement, which had an average SSA of 343 $m^2 kg^{-1}$.

Table 1. Chemical composition of cement and ceramic.

Chemical composition	Cement (%)	Ceramic (%)
SiO_2	20.47	61.72
Al_2O_3	5.90	22.31
CaO	59.64	6.67
Fe_2O_3	4.80	1.24
MgO	2.74	0.65
SO_3	2.08	0.07
Na_2O	0.80	0.96
K_2O	-	1.55
LOI	1.97	3.96

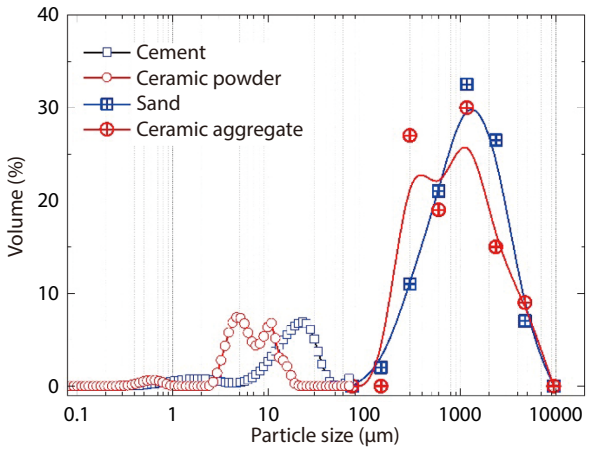

Fig. 1. Particle size distributions of cement, sand, and ceramic materials.

Particle size distribution analysis indicated that 99.98% of ceramic powder particles (by volume) and 58.20% of cement particles (by volume) possessed diameters below 10 μm. Another portion of the ceramics was crushed to produce fine aggregates with morphologies resembling natural sand, with their particle size distribution also depicted in Fig. 1.

Pore size distributions were characterized using dynamic vapor sorption (DVS) and mercury intrusion porosimetry (MIP), as shown in Fig. 2. The characteristic pore sizes were determined to be 1.05 μm for the ceramic aggregate and 5–8 nm for the ceramic powder. As shown in Fig. 3, scanning electron microscopy (SEM) imaging indicated irregular and angular particle morphologies for both ceramic powder and aggregate. Consistent with previous studies[14,23], quartz and mullite were identified as the primary mineral components of the ceramic material.

2.2. Sample preparation

Seven groups of cement-based mixtures were prepared, all maintaining a constant water-to-binder ratio (*w/b*) of 0.4 and incorporating five varying ceramic aggregate contents. Ceramic fine aggregate was tested at six substitution levels (0% to 100% in 20% increments) to cover the full replacement range of natural sand. The fixed 20% interval was adopted for systematic performance analysis. Performance trends were monitored continuously as ceramic content increased. The detailed mix proportions for each mixture are presented in Table 2. Following mixing, the fresh mortars

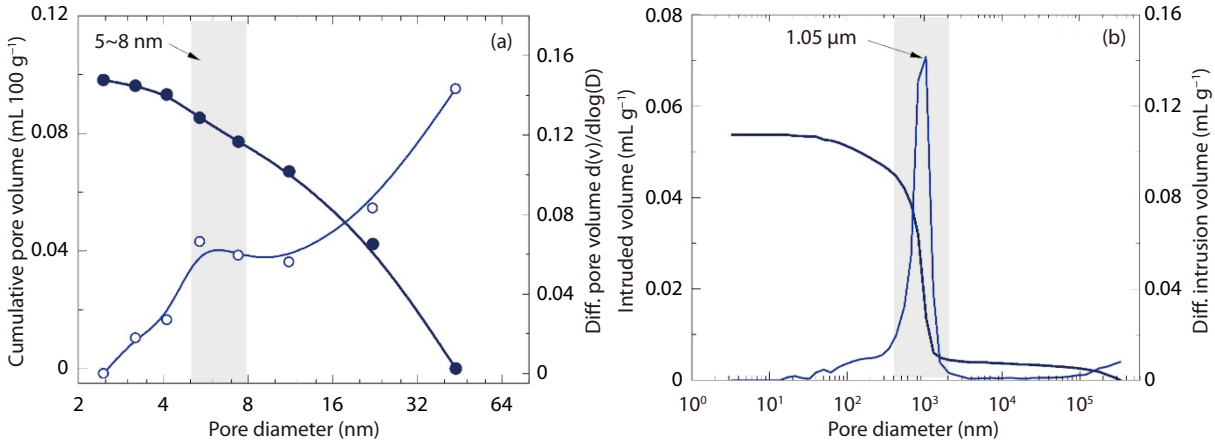

Fig. 2. Accumulative and differential pore size distributions: (a) ceramic powder measured by DVS and (b) ceramic aggregate measured by MIP.

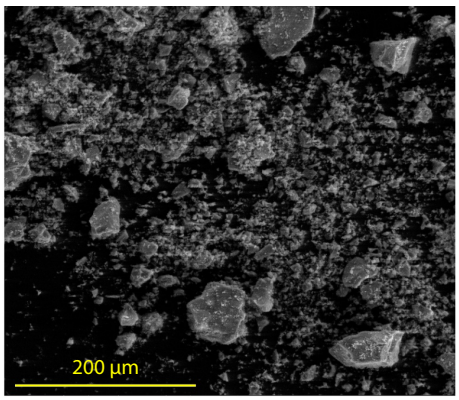

Fig. 3. SEM of ceramic particles.

were poured into steel prism moulds measuring 40 mm × 40 mm × 160 mm. The hardened specimens were demoulded at an age of 3 d and subsequently immersed in water for curing under controlled room conditions at 20 °C.

At curing ages of 7, 28, 90, and 180 d, specimens were retrieved from the water for further characterization. Mechanical tests were conducted on prism specimens to assess the strength development over time. In addition, granular samples with particle sizes ranging from 3 to 5 mm were obtained for MIP analysis. Powder samples were sieved to obtain a particle size fraction ranging from 200 to 300 μm for thermogravimetric (TG), DVS, and X-ray diffraction (XRD) analyses. To arrest further hydration and minimize carbonation, all crushed samples were immediately immersed in acetone prior to testing.

2.3. Evaluation of hydration reaction

TG and XRD analyses were employed to investigate the hydration products of cement-based materials incorporating ceramic powder. TG analysis allows the identification of various phases in cement pastes through controlled heating, enabling the observation of compositional evolution with hydration time. During the heating process, three distinct mass loss stages can be identified[24]: a low-temperature loss (20–150 °C), primarily due to the evaporation of pore water and partial dehydration of calcium silicate hydrate (C-S-H), as well as ettringite breakdown; a mid-temperature drop (400–500 °C), predominantly linked to the portlandite ($Ca(OH)_2$) decomposition; a high-temperature decline (600–700 °C), arising from the thermal decomposition of calcium carbonate ($CaCO_3$).

The extent of cement hydration can be assessed by quantifying the non-evaporable water (W_n) content, determined from the mass loss measured over the temperature interval of 150 °C to 1000 °C. This parameter W_n reflects the amount of water chemically bound in hydration products and thus offers a reliable means to evaluate how ceramic powder incorporation affects the kinetics and completeness of cement hydration, calculated as:

$$W_n = \left[\frac{m_{150} - m_{1000}}{m_{1000}} - \left(f_{ce} \cdot \mathrm{LOI}_{ce} + f_{cp} \cdot \mathrm{LOI}_{cp}\right)\right] \times 100\% \quad (1)$$

where f_{ce} and f_{cp} denote the mass proportions of cement and ceramic powder in binder, respectively; LOI_{ce} and LOI_{cp} are the loss on ignition of cement and ceramic powder, respec-

Table 2. Mix proportion of mortars.

Sample No.	Mix proportion(kg m^{-3})					CA substitution ratio (%)	CP substitution ratio (%)
	Cement	Water	Sand	Ceramic aggregate	Ceramic powder		
P0	624	250	1248	0	0	0	0
M0	499	241	1248	0	103	0	20
M2	489	236	998	224	101	20	20
M4	480	232	749	448	99	40	20
M6	469	226	499	672	97	60	20
M8	459	222	250	897	95	80	20
M10	449	217	0	1121	93	100	20

tively. According to the TG curves, the quantity of $Ca(OH)_2$ is derived based on the measured mass loss of water, multiplied by the molar mass ratio of $Ca(OH)_2$ to H_2O (i.e., 74.09/18.02 ≈ 4.11),

$$m_{CH} = \frac{74.09}{18.02}(m_{400} - m_{500}) \quad (2)$$

where the term ($m_{400} - m_{500}$) is the percentage mass loss observed between 400 °C and 500 °C when the thermal decomposition of $Ca(OH)_2$ takes place.

TG measurements were carried out using a NETZSCH STA 449 F5 simultaneous thermal analyzer. Prior to analysis, samples were finely ground and loaded into alumina crucibles. The heating program commenced at 25 °C and extended to 1000 °C at a linear ramp rate of 10 °C min^{-1}. To guarantee measurement reproducibility and reliability, triplicate tests were performed for each mixture. All experiments were conducted under a purified argon atmosphere (flow rate: 40 mL min^{-1}) to suppress any unwanted oxidation or carbonation reactions during the heating process.

XRD analysis was performed on a Rigaku SmartLab powder diffractometer employing CuKα radiation (wavelength λ = 0.15418 nm) as the X-ray source. The diffractometer was run at 40 kV and 30 mA, with an open attenuator configuration. Data collection spanned a 2θ range of 5° to 80° with a continuous scan speed of 10° min^{-1}. Phase identification and qualitative assessment of hydration phases were performed using HighScore Plus software for reliable peak indexing and phase matching.

2.4. Evaluation of pore structure

MIP is based on the physical relationship between applied pressure and intruded mercury volume into pores: higher pressures force mercury into progressively smaller pores. Assuming cylindrical pore geometry, the Washburn equation links the effective pore diameter (d_{MIP}) to the applied pressure (P_{MIP}) as $d_{MIP} = -4\gamma_m \cos\psi / P_{MIP}$, where γ_m = 0.485 N m^{-1} represents the surface tension of mercury, and ψ = 130° denotes the contact angle formed between mercury and the pore wall. By plotting the incremental volume of intruded mercury against the corresponding pore diameter, a volume-based pore size distribution (PSD) is constructed, enabling quantitative characterization of pore structure across the meso- to macropore range.

MIP tests were conducted with an AutoPore IV 9510 mercury porosimeter, which applies pressures from 3.5 kPa to 414 MPa, covering a pore size range of ~3 nm to 356 µm. The acquired intrusion curves enabled the extraction of key pore structure parameters: total open porosity, PSD spectra, SSA, average pore diameter, and threshold pore diameter. These parameters collectively provide a comprehensive quantitative insight into the pore structure of the cementitious materials.

An additional technique employed in this study for pore structure characterization is water vapor sorption isotherms (WVSI). WVSI measurements were carried out on a Surface Measurement Systems (UK) DVS-Adventure gravimetric sorption analyzer. Prior to testing, each sample was ground into particles ranging from 200 to 500 µm. To obtain a comprehensive understanding of the sorption behavior, mortar samples were subjected to various targeted relative humidity (RH) levels at each sorption stage. The temperature was maintained at 20 °C throughout the experiments. Mass equilibrium was considered to be achieved when the relative change in mass was less than 0.001% over a ten-minute interval, and this criterion was consistently applied across all measurements.

Equilibration during water vapor sorption typically took 3–7 d, depending on the target RH level and the kinetics of surface adsorption and capillary condensation within the porous mortar matrix. Once equilibrium was attained, the mass of the partially saturated mortar sample (m_{ads}) was recorded. The corresponding degree of water saturation (S) was then calculated as $S = (m_{ads} - m_d) / (m_s - m_d)$, where m_d and m_s represent the mass of the dry and fully saturated samples, respectively. The resulting isotherms describe the equilibrium relationship between water uptake (expressed either as gravimetric moisture content or saturation degree) and RH. Furthermore, by applying the Kelvin equation, these isotherms can be converted into a pore size distribution. Specifically, the relationship between the pore diameter (d) and RH (h), where d reflects the smallest pore radius capable of sustaining capillary condensation at a given h, is determined as:

$$d = d_K + 2\tau, d_K = -\frac{4\gamma_{lg} - V_{mol}}{RT \ln h} \quad (3)$$

where d_K is the Kelvin pore diameter; R (J mol^{-1} K^{-1}), T (K), V_{mol} (m^3 mol^{-1}), γ_{lg} (N m^{-1}), and τ (nm) denote the universal gas constant, absolute temperature, molar volume of water, surface tension at the water-vapor interface, and the effective thickness of the adsorbed water film on the pore surface, respectively. The parameter τ is RH-dependent, and the model proposed by Hagymassy et al.[25] is employed as follows:

$$\tau = 0.836h + 0.0626 + \frac{0.0236}{1.015 - h} \quad (4)$$

By applying Eqs. (3) and (4), the PSDs of porous materials can be derived from WVSI data.

2.5. Evaluation of mechanical properties

Mechanical tests followed the Chinese standard[26]. Flexural strength was determined via four-point bending tests conducted on a WHY-300/10 universal testing system (Hualong Instrument Co., Ltd., Shanghai). A four-point loading configuration was adopted, featuring a support span of 100 mm and an inner loading span of 40 mm. Prism specimens were carefully positioned and aligned within the fixture to ensure uniform stress distribution across the mid-span region. Loading was applied at a constant rate of 50 N s^{-1} until failure. The maximum load at failure was recorded for subsequent flexural strength calculation.

For each mixture at each curing age, three replicate four-point bending tests were performed, yielding six half-prism specimens. These half-prisms were subsequently subjected to compressive loading using the same testing machine under a controlled loading rate of 2.4 kN s^{-1}. All measured values

were averaged to obtain statistically representative results for both flexural and compressive strengths.

3. Compressive strength of the mortars

Fig. 4 displays the measured compressive strength values of all mortar mixtures across the investigated curing ages. The substitution of cement with ceramic powder leads to a decline in the early-age mechanical strength of mortars, particularly within the initial 28-day hydration period. Contrary to the original description of strength reduction, the data in Fig. 4a indicate a clear and consistent increase in compressive strength with higher ceramic aggregate substitution ratios across all curing ages. For instance, at 28 d, the compressive strength rises progressively from 55.1 MPa for M0 (0% substitution) to 60.6 MPa for M6 (60% substitution), representing an increase of 10%. Similarly, at 90 d, the strength improves from 68.0 MPa to 73.1 MPa, a gain of 7.5%. These observations suggest that replacing natural sand with ceramic aggregate (up to 60%) leads to a measurable improvement in compressive strength. However, beyond 60% replacement level, further increases in ceramic aggregate content result in a gradual decline in strength.

The flexural strength results, shown in Fig. 4b, follow a similar increasing trend. At 28 d, flexural strength increases from 6.2 MPa to 8.3 MPa as the ceramic aggregate content rises from 0% to 80%, corresponding to a 33.9% enhancement. At 180 d, the flexural strength improves from 7.7 MPa to 9.9 MPa, a 28.6% increase. These findings indicate that the incorporation of ceramic aggregate not only maintains but also improves both compressive and flexural performance, particularly at longer curing durations.

The findings are consistent with previous investigations involving various types of ceramic aggregates[27–29]. For instance, Torkittikul and Chaipanich[29] reported an 18.9% increase in compressive strength for mortar mixtures incorporating 50% ceramic aggregates. Similarly, Siddique et al.[30] observed enhanced compressive strength when 40% to 60% of fine natural aggregates were replaced with ceramic aggregates.

The observed improvement in mechanical performance is primarily attributed to the surface characteristics of the ceramic aggregates. A rougher aggregate texture enhances the mechanical interlock and bond strength at the interfacial transition zone (ITZ) between the cementitious matrix and aggregate particles[31]. Additionally, the pozzolanic activity of ceramic aggregates contributes to the generation of a more compact and stable C-S-H phase, further promoting strength development[30]. However, a quasi-linear reduction in both compressive and flexural strengths is observed when the ceramic aggregate replacement ratio exceeds 60%. This decline is likely attributable to the angular and irregular morphology of ceramic aggregates, which adversely affects the workability and compaction efficiency of the fresh mixture. The resulting increase in internal porosity and imperfect packing density may compromise the overall mechanical integrity of the hardened mortar.

4. Hydration reaction and microstructure

4.1. Chemical activity effects

Fig. 5 presents the TG-derived mass loss profiles of ceramic powder and cement pastes. Three distinct stages are identified: phase A corresponds to the dehydration and loss of physically bound water; phase B reflects $Ca(OH)_2$ decomposition; and phase C corresponds to $CaCO_3$ decarbonation.

The non-evaporable water (W_n) content, which reflects the extent of hydration, is presented in Table 3. For the plain cement paste (P0), the degree of hydration reaches approximately 62% at 7 d and increases to 89% at 180 d, calculated according to Lam et al.[32]. Notably, P0 exhibits a higher absolute content compared to mixtures containing ceramic powder. However, when normalized per 100 g of cement, the content in the ceramic-containing paste (M0) exceeds that in P0, as shown in Table 3. This observation aligns with findings reported by Pavlík et al.[33]. The comparatively higher value

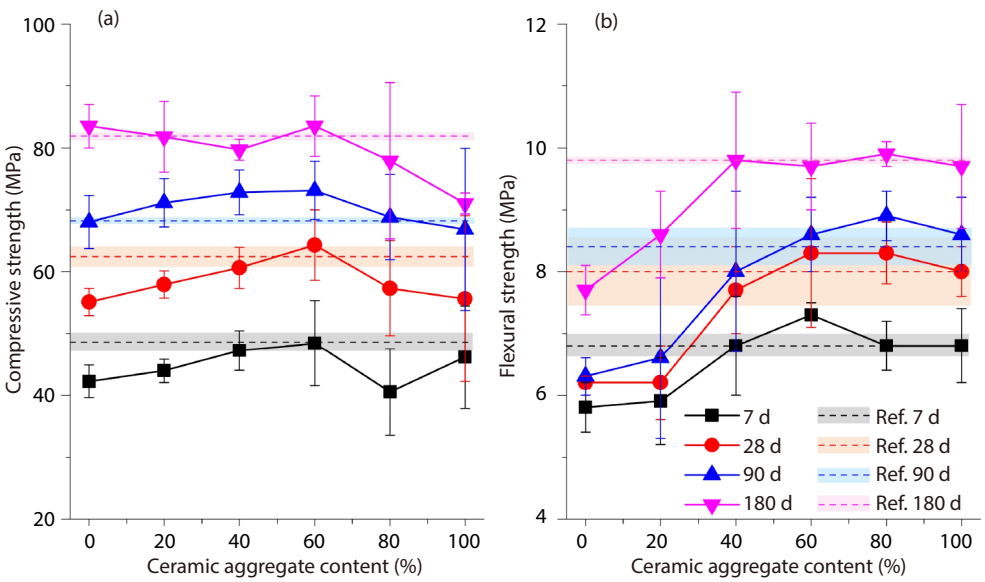

Fig. 4. Compressive strength test and flexural strength test values of all mortar mixtures.

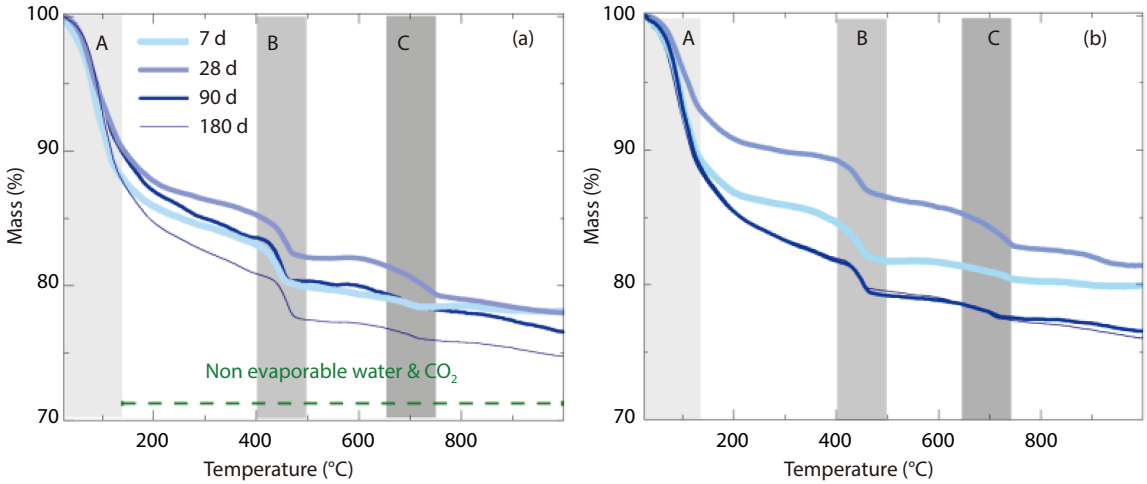

Fig. 5. TG spectra for (a) the P0 sample and (b) the M0 sample at different ages, highlighting the characteristic decomposition stages A, B, and C.

Table 3. Non-evaporable water content of ceramic powder/cement pastes.

Sample No.	W_n content (%)			
	7 d	28 d	90 d	180 d
P0	14.19	17.03	19.26	20.44
M0 (based on ignited weight)	13.24	14.89	18.32	18.06
M0 (per 100 g of cement)	16.55	18.61	22.90	22.57

observed in M0 arises from two contributing factors: the pozzolanic reaction of the ceramic powder, which generates additional hydration products, and the enhanced hydration of cement in blended systems due to an increased effective water-to-cement (*w/c*) ratio, as suggested by Wang et al.[34]. The latter effect arises because partially replacing cement with ceramic powder dilutes the cement concentration, thereby raising the available *w/c* ratio and consequently accelerating the hydration kinetics.

The calcium hydroxide ($Ca(OH)_2$) content, determined using Eq. 2 and summarized in Table 4, exhibits distinct trends across mixtures. For P0, the $Ca(OH)_2$ content increases with curing age, consistent with the progressive hydration of cement. In contrast, for the ceramic-containing sample M0, the $Ca(OH)_2$ content declines as curing age advances. This decrease reflects the ongoing pozzolanic reaction, wherein $Ca(OH)_2$ is progressively consumed to generate supplementary C-S-H phase. At 7 and 28 d, M0 (per 100 g of cement) shows a higher relative $Ca(OH)_2$ content than P0, suggesting that the pozzolanic reaction becomes more pronounced only after an initial period. Between 7 and 28 d, the significantly slower growth rate of $Ca(OH)_2$ content provides clear evidence of ceramic powder reactivity. By 90 d, hydration products are expected to form extensively on the surfaces of ceramic powder particles, accompanied by further $Ca(OH)_2$ consumption. This process strengthens the interfacial bonding between cement and ceramic powder, as well as among ceramic powder particles themselves, thereby enhancing the long-term mechanical performance of the composite material.

Table 4. $Ca(OH)_2$ content of ceramic powder/cement pastes.

Sample No.	$Ca(OH)_2$ content (m_{CH}, %)			
	7 d	28 d	90 d	180 d
P0	16.62	20.23	18.61	19.95
M0 (based on ignited weight)	16.19	17.24	14.95	14.70
M0 (per 100 g of cement)	20.24	21.55	18.69	18.37

Fig. 6 displays the XRD profiles of the samples, revealing the primary crystalline phases: $Ca(OH)_2$, C-S-H, ettringite, C_3S, C_2S, and SiO_2. In comparison with the plain cement paste (P0), the ceramic-containing sample (M0) exhibits distinct diffraction peaks corresponding to SiO_2, attributable to the high silica content of the ceramic powder. No other significant differences in phase composition are observed between the two groups.

At each curing age, the strongest $Ca(OH)_2$ diffraction peaks consistently appear in the P0 group. At 7 d, the difference in peak intensity between P0 and M0 is relatively small; however, as the curing age increases, this difference becomes more pronounced. This trend indicates that in the M0 samples, the rate of $Ca(OH)_2$ consumption exceeds that of its generation. The reduction in $Ca(OH)_2$ content correlates with an increased degree of pozzolanic reaction of the ceramic powder. Furthermore, the intensity of this reaction increases with prolonged curing, reflecting the progressive

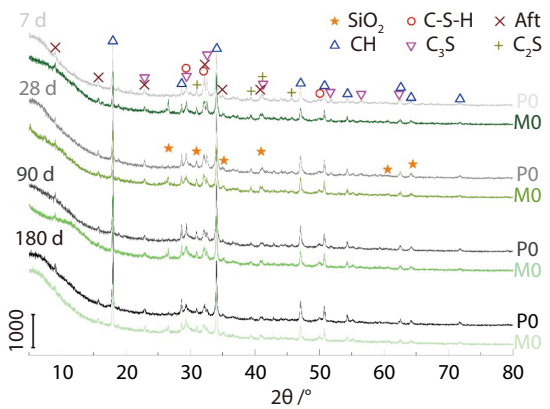

Fig. 6. XRD spectra of P0 and M0 containing 20% ceramic powder by mass at various ages.

pozzolanic activity of the ceramic material.

4.2. Physical filling effects

Fig. 7a illustrates the WVSI data, expressed as the volume of adsorbed water per unit mass of dry mortar. Each data point represents the mean value obtained from three parallel measurements conducted at a given RH level. As RH increases to 60%, the equilibrium water uptake of all mortar specimens exhibits a gradual yet distinctly nonlinear increase, while the adsorption isotherm steepens progressively with increasing RH. This slow uptake at low RH levels is attributed to the presence of nanostructural units within the C-S-H phase, which possess abundant interlayer spaces capable of accommodating water molecules[35]. In the higher RH range, a more pronounced increase in sorption content is observed. This accelerated water accumulation is associated with the filling of relatively large voids—such as those spaces between sand grains, micro-fillers (e.g., ceramic powder), residual unhydrated cement clinkers, and microcrystalline hydration products including calcium hydroxide (CH) and ettringite—as well as nanoscale hydrates generated during the cement hydration process[36].

Fig. 7a further indicates that the overall shape of the sorption isotherms remains largely unaffected by the incorporation of ceramic aggregate. However, the equilibrium water sorption content at RH = 0.95 exhibits a decreasing trend with increasing ceramic aggregate content. In contrast, when the results are expressed in terms of liquid saturation degree (Fig. 7b), the inclusion of ceramic aggregates leads to higher saturation levels at equivalent RH values. This observation suggests that ceramic aggregates introduce additional large pores, beyond the size range typically accessible via capillary condensation at RH = 0.95, capable of storing more water. Such pores may originate from intrinsic porosity within the ceramic particles, as well as from voids generated during mixing and casting.

As shown in Fig. 7a, the WVSI curves nearly overlap when RH is below 0.4, indicating that the nanoscale C-S-H structures remain largely unchanged across different ceramic replacement ratios. At low RH (< 0.4), water adsorption occurs predominantly within the nanoscale gel pores of C-S-H, with the extent and kinetics governed by the surface hydrophilicity of hydration products. At high RH (> 0.4), capillary condensation becomes the dominant mechanism, with water occupying larger capillary pores; this shift is more directly influenced by the ceramic aggregate content, reflecting its role in modifying the larger-scale pore structure of the composite material.

To further investigate the pore structure characteristics, the pore size distributions (PSDs) obtained from MIP and WVSI are presented in Figs. 8 and 9, respectively. The pore size distributions derived from MIP and WVSI display distinct characteristics: WVSI yields a differential pore size distribution (DPSD) curve dominated by a single peak, whereas MIP reveals a bimodal pattern. This divergence likely arises from the ink-bottle effect in MIP, wherein measured intrusion pressures are governed by the pore throats rather than the pore bodies, and potential microstructural damage during high-pressure intrusion. In contrast, WVSI probes pore volumes through non-destructive, equilibrium water vapor adsorption, thereby offering a more direct representation of the actual pore network.

As shown in Fig. 8a, the MIP-derived cumulative intrusion curves exhibit a slow increase in mercury uptake for pore sizes above 30 nm, followed by a sharp rise as the pressure increases to access pores down to the minimum detectable size of approximately 3 nm. The initial gradual intrusion is attributed to the filling of surface topographic defects on the fractured sample, such as open voids, microcracks, cavities, and interfacial gaps between ceramic and cement grains[37]. The subsequent rapid intrusion corresponds to the forced penetration of mercury into extensive capillary networks and gel pores under elevated pressures. Notably, the total intruded mercury volume increases with higher ceramic aggregate content, indicating greater overall porosity.

The DPSDs from MIP (Fig. 8b) and WVSI (Fig. 9b) provide further insight into pore structure modifications induced by ceramic aggregate. Most pores fall within the range of 3–60 nm in MIP and 2–30 nm in WVSI. The MIP-derived DPSDs

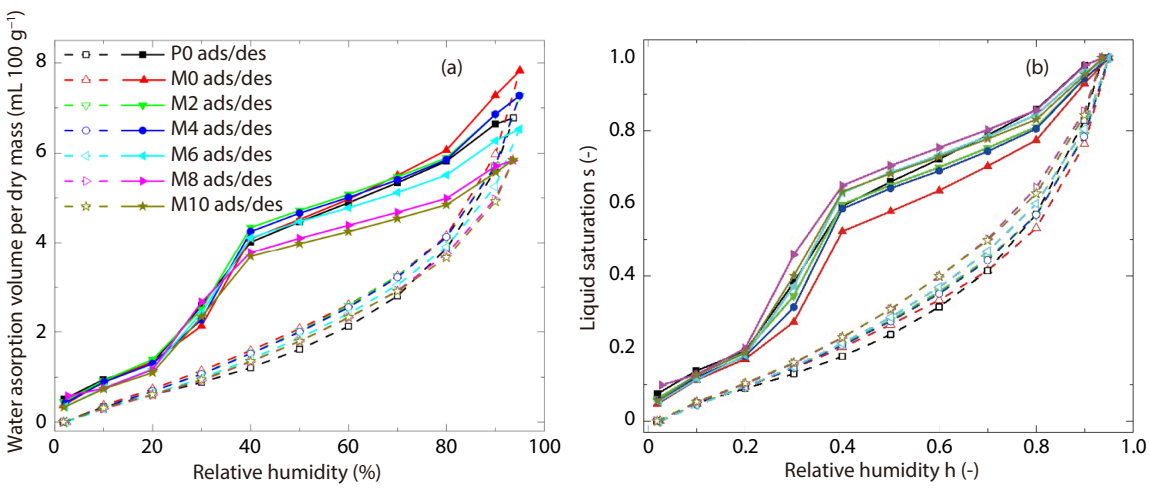

Fig. 7. (a) Equilibrium water contents per 100 g of dry mortar and (b) pore liquid saturations of the ceramic mortars measured at different RH levels in the WVSI experiments.

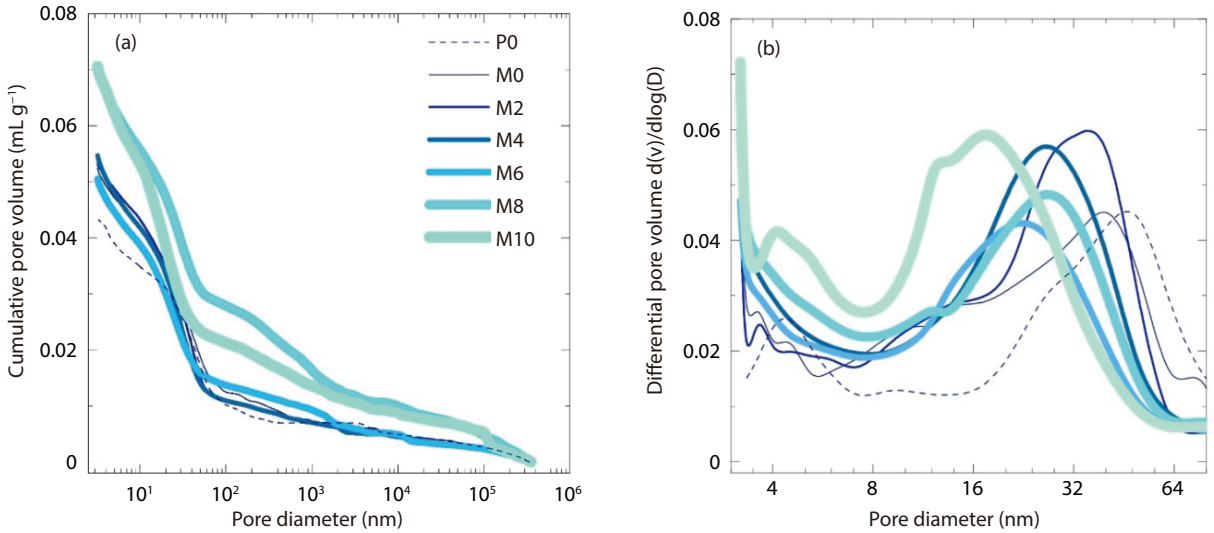

Fig. 8. Pore size distributions tested by MIP. (a) Cumulative pore size distribution and (b) differential pore size distribution.

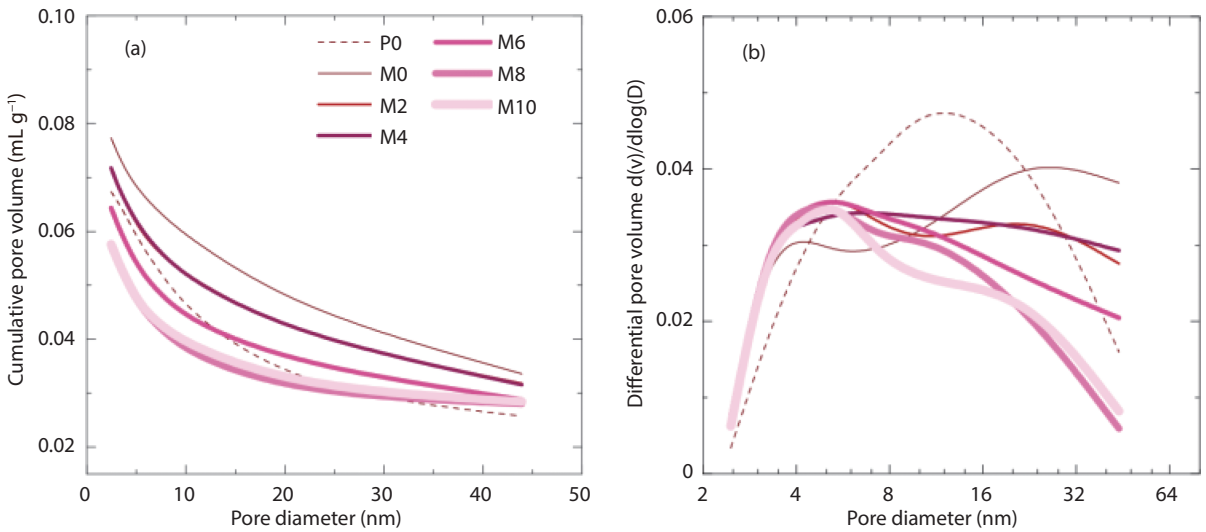

Fig. 9. Pore size distributions tested by WVSI. (a) Cumulative pore size distribution and (b) differential pore size distribution.

reveal two distinct peaks: a broad peak spanning 8–30 nm corresponding to large gel pores and fine capillaries, and a sharper, lower-intensity peak centered at 3–4 nm, which reflects small gel pores within C-S-H interlayer spaces[38,39]. Adding 20% ceramic powder enhances the small pore peak intensity in WVSI DPSDs (Fig. 9b). Conversely, raising the proportion of CA leads to a marked reduction in the intensity of the coarse-pore peak (8–30 nm). Interestingly, with increasing ceramic content, the fraction of finer capillaries decreases, while the proportion of larger gel pores increases, indicating a nanoscale pore coarsening effect induced by ceramic incorporation.

5. Conclusions

Drawing upon the experimental findings and analyses outlined above, the following key conclusions are established.

(1) A decline in the early-age mechanical strength of mortars was observed when natural sand was substituted with ceramic aggregate, particularly within the initial 28-day hydration period. However, with extended curing durations, the negative impact on compressive strength becomes progressively less significant. In mixtures containing high volumes of ceramic aggregate, prolonged curing allows for partial recovery and even improvement in mechanical properties, suggesting that the long-term performance of such mortars is not inherently compromised. This behavior is consistent with observations reported for other supplementary cementitious materials, where pozzolanic reactions contribute to strength development at later ages.

(2) The higher relative non-evaporable water content in cement pastes incorporating ceramic powder arises from two synergistic mechanisms. Firstly, the pozzolanic activity of the ceramic powder contributes to the formation of additional C-S-H phase, thereby increasing the total hydration product volume per unit mass of cement. Secondly, substituting a portion of the cement with ceramic powder, whose reactivity is low, effectively raises the *w/c* ratio available for the remaining clinker, thereby enhancing its degree of hydration, which is commonly termed the dilution effect. As curing age increases, the $Ca(OH)_2$ content decreases, reflecting its ongo-

ing consumption via pozzolanic reaction with ceramic powder. This $Ca(OH)_2$ consumption is directly associated with the formation of secondary C-S-H phase, which strengthens the interfacial bonding between cement and ceramic particles, as well as among ceramic powder particles themselves.

(3) The microstructure becomes more densified and homogeneous over time. This microstructural refinement not only compensates for the early-age strength loss but also contributes to a substantial enhancement in long-term compressive strength, underscoring the potential of ceramic wastes for sustainable construction applications.

Acknowledgements

The authors acknowledge the Fundamental Research Funds for the Central Universities, China (No. 2652023022), the Natural Science Foundation of Jiangxi Province, China (No. 20202ACBL214018), and the Natural Science Foundation of China (No. 51808218).

Data availability

The data supporting the findings of this study are available within the article. Additional data are available from the corresponding author upon reasonable request.

Declaration of competing interest

The authors declare that they have no known competing financial interests or personal relationships that could have appeared to influence the work reported in this paper.

Author contribution statement

Shibo Sun: Data curation, Writing – original draft. **Haoran Jia:** Data curation, Methodology. **Xiaochuan Hu:** Data curation, Formal analysis. **Linsheng Li:** Resources, Validation. **Xinyu Wang:** Data curation, Investigation. **Sha Qing:** Software, Visualization. **Le Li:** Conceptualization, Methodology, Writing – review & editing, Supervision, Data curation, Writing – original draft, Project administration, Funding acquisition.

Use of AI statement

None.

References

[1] Miao, C., Mu, S. Development and prospect of concrete technology in China. *Materials Reports: Solidwaste and Ecomaterials*, **2025**: 9520001. https://doi.org/10.26599/mrse.2025.9520001.

[2] Oggioni, G., Riccardi, R., Toninelli, R. Eco-efficiency of the world cement industry: A data envelopment analysis. *Energy Policy*, **2011**, 39(5): 2842–2854. https://doi.org/10.1016/j.enpol.2011.02.057.

[3] Wang, L., Wu, C., Li, K., et al. A reactive transport model for concrete exposed to cyclic wetting/drying: Salt crystallization, carbonation, leaching, and beyond. *Transport in Porous Media*, **2025**, 152(5): 32. https://doi.org/10.1007/s11242-025-02175-3.

[4] Ma, J., Chen, Z., Yu, K., et al. Resource utilization of municipal solid waste incineration residues in cement-based materials: A review. *Materials Reports: Solidwaste and Ecomaterials*, **2025**: 9520007. https://doi.org/10.26599/mrse.2025.9520007.

[5] Zeng, Q., Li, K., Fen-chong, T., et al. Pore structure characterization of cement pastes blended with high-volume fly-ash. *Cement and Concrete Research*, **2012**, 42(1): 194–204. https://doi.org/10.1016/j.cemconres.2011.09.012.

[6] Luo, Q., Zhang, X., Bai, Y., et al. Purifying marine clay for the preparation of LC^3. *Materials Reports: Solidwaste and Ecomaterials*, **2025**: 9520008. https://doi.org/10.26599/mrse.2025.9520008.

[7] Gautam, L., Maaze, M. R., Sharma, K. V. Optimizing self-compacting concrete with bone China ceramic and granite waste for improved mechanical and durability properties. *Journal of Materials in Civil Engineering*, **2025**, 37(2): 04024525. https://doi.org/10.1061/jmcee7.mteng-18929.

[8] Liu, Y., Wang, H., Hao, Y., et al. Effect of pretreatments of MSWIFA on the properties and microstructural mechanisms of OPC-MSWIFA-GGBFS composite binders. *Journal of Building Engineering*, **2026**, 120: 115454. https://doi.org/10.1016/j.jobe.2026.115454.

[9] Yang, Y., Ren, H., Ma, X. Dimensional engineering of fly ash-grown carbon nanomaterials for sustainable cement reinforcement. *Materials Reports: Solidwaste and Ecomaterials*, **2025**: 9520021. https://doi.org/10.26599/mrse.2025.9520021.

[10] Joshi, T., Dave, U., Raman, S. N., et al. Evaluation of strength, durability, and microstructural properties of concrete with ceramic waste aggregates. *Construction and Building Materials*, **2025**, 491: 142733. https://doi.org/10.1016/j.conbuildmat.2025.142733.

[11] Korat, A., Amin, M., Tahwia, A. M. A comprehensive assessment of ceramic wastes in ultra-high-performance concrete. *Innovative Infrastructure Solutions*, **2025**, 10(1): 28. https://doi.org/10.1007/s41062-024-01806-w.

[12] Li, L., Liu, W., Zeng, Q., et al. Sustainable reuse of household ceramic wastes as a substitute of cement and natural sand in construction materials: Mechanical, transport, and microstructural properties. *Case Studies in Construction Materials*, **2025**, 22: e04708. https://doi.org/10.1016/j.cscm.2025.e04708.

[13] Nepomuceno, M. C. S., Isidoro, R. A. S., Catarino, J. P. G. Mechanical performance evaluation of concrete made with recycled ceramic coarse aggregates from industrial brick waste. *Construction and Building Materials*, **2018**, 165: 284–294. https://doi.org/10.1016/j.conbuildmat.2018.01.052.

[14] Li, L., Liu, Z., Liu, W., et al. Microstructure and transport properties of cement mortar made with recycled fine ceramic aggregates. *Developments in the Built Environment*, **2025**, 22: 100643. https://doi.org/10.1016/j.dibe.2025.100643.

[15] Ali Hashim, A., Anaee, R., Nasr, M. S., et al. Mechanical properties, corrosion resistance and microstructural analysis of recycled aggregate concrete made with ceramic wall waste and ultrafine ceria. *Journal of Materials Research and Technology*, **2025**, 36: 627–640. https://doi.org/10.1016/j.jmrt.2025.03.154.

[16] Pokorný, J., Fořt, J., Pavlíková, M., et al. Application of mixed ceramic powder in cement based composites. *Advanced Materials Research*, **2014**, 1054: 177–181. https://doi.org/10.4028/www.scientific.net/amr.1054.177.

[17] Vejmelková, E., Koňáková, D., Kulovaná, T., et al. Mechanical and thermal properties of moderate-strength concrete with ceramic powder used as supplementary cementitious material. *Advanced Materials Research*, **2014**, 1054: 194–198. https://doi.org/10.4028/www.scientific.net/amr.1054.194.

[18] Heidari, A., Tavakoli, D. A study of the mechanical properties of ground ceramic powder concrete incorporating nano-SiO_2 particles. *Construction and Building Materials*, **2013**, 38: 255–264. https://doi.org/10.1016/j.conbuildmat.2012.07.110.

[19] Yang, C., Xu, X., Lei, Z., et al. Enhancing mechanical properties of

three-dimensional concrete at elevated temperatures through recycled ceramic powder treatment methods. *Journal of Materials Research and Technology*, **2024**, 31: 434–446. https://doi.org/10.1016/j.jmrt.2024.06.036.

[20] Zhang, L., Shen, H., Xu, K., et al. Effect of ceramic waste tile as a fine aggregate on the mechanical properties of low-carbon ultrahigh performance concrete. *Construction and Building Materials*, **2023**, 370: 130595. https://doi.org/10.1016/j.conbuildmat.2023.130595.

[21] Cheng, Y. H., Huang, F., Liu, R., et al. Test research on effects of waste ceramic polishing powder on the permeability resistance of concrete. *Materials and Structures*, **2016**, 49(3): 729–738. https://doi.org/10.1617/s11527-015-0533-6.

[22] Cheng, Y., Huang, F., Li, G. L., et al. Test research on effects of ceramic polishing powder on carbonation and sulphate-corrosion resistance of concrete. *Construction and Building Materials*, **2014**, 55: 440–446. https://doi.org/10.1016/j.conbuildmat.2014.01.023.

[23] Li, L., Liu, W., You, Q., et al. Waste ceramic powder as a pozzolanic supplementary filler of cement for developing sustainable building materials. *Journal of Cleaner Production*, **2020**, 259: 120853. https://doi.org/10.1016/j.jclepro.2020.120853.

[24] Trník, A., Scheinherrová, L., Medveď, I., et al. Simultaneous DSC and TG analysis of high-performance concrete containing natural zeolite as a supplementary cementitious material. *Journal of Thermal Analysis and Calorimetry*, **2015**, 121(1): 67–73. https://doi.org/10.1007/s10973-015-4546-8.

[25] Hagymassy, J., Brunauer, S., Mikhail, R. S. Pore structure analysis by water vapor adsorption I. t-Curves for water vapor. *Journal of Colloid and Interface Science*, **1969**, 29(3): 485–491. https://doi.org/10.1016/0021-9797(69)90132-5.

[26] Ministry of Housing and Urban-Rural Development of the People's Republic of China, State Administration for Market Regulation. Standard for Test Method of Concrete Physical and Mechanical Properties. GB/T 50081-2019, **2019**.

[27] Rashid, K., Razzaq, A., Ahmad, M., et al. Experimental and analytical selection of sustainable recycled concrete with ceramic waste aggregate. *Construction and Building Materials*, **2017**, 154: 829–840. https://doi.org/10.1016/j.conbuildmat.2017.07.219.

[28] Gonzalez-Corominas, A., Etxeberria, M. Properties of high performance concrete made with recycled fine ceramic and coarse mixed aggregates. *Construction and Building Materials*, **2014**, 68: 618–626. https://doi.org/10.1016/j.conbuildmat.2014.07.016.

[29] Torkittikul, P., Chaipanich, A. Utilization of ceramic waste as fine aggregate within Portland cement and fly ash concretes. *Cement and Concrete Composites*, **2010**, 32(6): 440–449. https://doi.org/10.1016/j.cemconcomp.2010.02.004.

[30] Siddique, S., Shrivastava, S., Chaudhary, S. Influence of ceramic waste as fine aggregate in concrete: Pozzolanic, XRD, FT-IR, and NMR investigations. *Journal of Materials in Civil Engineering*, **2018**, 30(9): 04018227. https://doi.org/10.1061/(asce)mt.1943-5533.0002438.

[31] Zegardło, B., Szeląg, M., Ogrodnik, P. Ultra-high strength concrete made with recycled aggregate from sanitary ceramic wastes–The method of production and the interfacial transition zone. *Construction and Building Materials*, **2016**, 122: 736–742. https://doi.org/10.1016/j.conbuildmat.2016.06.112.

[32] Lam, L., Wong, Y. L., Poon, C. S. Degree of hydration and gel/space ratio of high-volume fly ash/cement systems. *Cement and Concrete Research*, **2000**, 30(5): 747–756. https://doi.org/10.1016/S0008-8846(00)00213-1.

[33] Pavlík, Z., Trník, A., Kulovaná, T., et al. DSC and TG analysis of a blended binder based on waste ceramic powder and Portland cement. *International Journal of Thermophysics*, **2016**, 37(3): 32. https://doi.org/10.1007/s10765-016-2043-3.

[34] Wang, Q., Wang, D., Chen, H. The role of fly ash microsphere in the microstructure and macroscopic properties of high-strength concrete. *Cement and Concrete Composites*, **2017**, 83: 125–137. https://doi.org/10.1016/j.cemconcomp.2017.07.021.

[35] Babaee, M., Castel, A. Water vapor sorption isotherms, pore structure, and moisture transport characteristics of alkali-activated and Portland cement-based binders. *Cement and Concrete Research*, **2018**, 113: 99–120. https://doi.org/10.1016/j.cemconres.2018.07.006.

[36] Bullard, J. W., Jennings, H. M., Livingston, R. A., et al. Mechanisms of cement hydration. *Cement and Concrete Research*, **2011**, 41(12): 1208–1223. https://doi.org/10.1016/j.cemconres.2010.09.011.

[37] Zeng, Q., Wang, X., Yang, P., et al. Tracing mercury entrapment in porous cement paste after mercury intrusion test by X-ray computed tomography and implications for pore structure characterization. *Materials Characterization*, **2019**, 151: 203–215. https://doi.org/10.1016/j.matchar.2019.02.014.

[38] Jennings, H. M. Refinements to colloid model of C-S-H in cement: CM-II. *Cement and Concrete Research*, **2008**, 38(3): 275–289. https://doi.org/10.1016/j.cemconres.2007.10.006.

[39] Powers, T. C. Structure and physical properties of hardened Portland cement paste. *Journal of the American Ceramic Society*, **1958**, 41(1): 1–6. https://doi.org/10.1111/j.1151-2916.1958.tb13494.x.

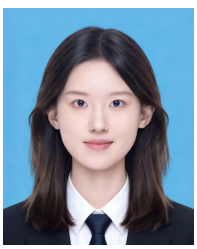

Shibo Sun is an undergraduate at the China University of Geosciences, Beijing, set to begin master's studies in the upcoming academic year. Her research applies enzymatic mineralization to precipitate calcium carbonate in concrete for autonomous microcrack repair.

Haoran Jia is currently a master's student at the China University of Geosciences, Beijing. His research focuses on the utilization of industrial solid wastes and the mechanical behavior and long-term durability of green construction materials.

Le Li is an associate professor and doctoral supervisor at the China University of Geosciences, Beijing. She obtained her PhD from Tsinghua University. Her research interests include long-term durability of concrete, self-healing mechanisms in cementitious systems, and advanced waste recycling technologies.